



Fast Fourier ptychographic quantitative phase microscopy for in vitro label-free imaging

RUOFEI WU,¹  ZICONG LUO,¹  MINGDI LIU,¹ HAIQI ZHANG,¹ JUNRUI ZHEN,¹ LISONG YAN,² JIAXIONG LUO,¹ AND YANXIONG WU^{1,3,*}

¹*School of Physics and Optoelectronic Engineering, Foshan University, Foshan 528000, China*

²*School of Optical and Electronic Information, Huazhong University of Science and Technology, Wuhan 430074, China*

³*Ji Hua Laboratory, Foshan, Guangdong 528200, China*

*wuyanxiong@fosu.edu.cn

Abstract: Quantitative phase microscopy (QPM) is indispensable in biomedical research due to its advantages in unlabeled transparent sample thickness quantification and obtaining refractive index information. Fourier ptychographic microscopy (FPM) is among the most promising QPM methods, incorporating multi-angle illumination and iterative phase recovery for high-resolution quantitative phase imaging (QPI) of large cell populations over a wide field-of-view (FOV) in a single pass. However, FPM is limited by data redundancy and sequential acquisition strategies, resulting in low imaging efficiency, which in turn limits its real-time application in in vitro label-free imaging. Here, we report a fast QPM based on Fourier ptychography (FQP-FPM), which uses an optimized annular downsampling and parallel acquisition strategy to minimize the amount of data required in the front end and reduce the iteration time of the back-end algorithm (3.3% and 4.4% of conventional FPM, respectively). Theoretical and data redundancy analyses show that FQP-FPM can realize high-throughput quantitative phase reconstruction at thrice the resolution of the coherent diffraction limit by acquiring only ten raw images, providing a precondition for in vitro label-free real-time imaging. The FQP-FPM application was validated for various in vitro label-free live-cell imaging. Cell morphology and subcellular phenomena in different periods were observed with a synthetic aperture of 0.75 NA at a 10× FOV, demonstrating its advantages and application potential for fast high-throughput QPI.

© 2023 Optica Publishing Group under the terms of the [Optica Open Access Publishing Agreement](#)

1. Introduction

In vitro label-free imaging enables the observation of the internal structure of cells in a non-invasive manner and is a key technology for probing their physiological properties [1]. In the biomedical field, most biological samples exhibit spatially inhomogeneous thickness and refractive index distributions, which result in most of the information being embedded in the phase rather than in the amplitude [2]. However, limitations due to the sampling frequency of the human eye and camera, as well as the imaging mechanism of conventional optical microscopy, hinder observing “phase samples” with sufficiently high contrast to effectively obtain phase information [3]. This can be achieved via invasive methods, such as chemical staining or fluorescent labeling, to generate sufficiently strong light absorption contrast for observational purposes, such as in stimulated emission depletion microscopy [4,5] and photoactivated localization microscopy [6,7], both of which were awarded the Nobel Prize in Chemistry in 2014, and stochastic optical reconstruction microscopy [8,9]. Nevertheless, these methods suffer from phototoxicity and photobleaching, which inevitably adversely affect the structure and activity of cells. Therefore, realizing unstained or unlabeled phase imaging is of great significance to the field of biomedicine.

Quantitative phase microscopy (QPM) is a cross-combination of optical imaging principles and computational methods that enables quantitative phase reconstruction of biological samples

in a non-invasive manner and has become an important tool for biomedical research [10,11]. The main existing QPM methods include digital holography microscopy (DHM) [12,13], structured illumination microscopy (SIM) [14,15], spatial and gradient light interference microscopy [16,17], transport of intensity equation (TIE) [18,19], quantitative differential phase-contrast imaging (DPC) [20,21], and Fourier ptychographic microscopy (FPM) [22–25]. DH, SIM, SLIM and GLIM are all interferometric QPMs that rely on highly coherent light sources or complex interferometric light paths to achieve quantitative phase imaging (QPI), which is susceptible to environment or scattering noise and difficult to operate. Non-interferometric QPM methods, such as TIE and DPC, are simpler because they inversely solve the phase distribution by measuring only the intensity distribution of the optical wavefield, showing no advantage. However, in the aforementioned QPM methods, the maximum achievable imaging resolution remains subject to the incoherent diffraction limit (twice the coherent diffraction limit) owing to the configuration of the illumination conditions. A trade-off between the field-of-view (FOV) and imaging resolution in optical microscopy is difficult, therefore limiting the development of high-throughput microscopic imaging techniques. FPM can overcome this limitation by illuminating the sample with plane waves generated by an angularly varying tilted light source, moving the frequency information that originally exceeds the numerical aperture of the objective lens (NA_{obj}) within the objective lens bandwidth [26], utilizing an iterative phase restoration algorithm to recover the high-frequency information of the sample and expand the spectrum [23,27,28], and ultimately reconstructing, in an elegant and ingenious manner, a sample with a large-FOV high-resolution complex amplitude image. The synthesized NA is equivalent to the sum of NA_{obj} and the illumination NA (NA_{ill}). Therefore, compared with that of other QPM methods, the imaging resolution of FPM can reach several times the coherent diffraction limit of the imaging system while still retaining the large FOV and depth of field of the low-magnification objective [29], thereby resolving the conflict between the resolution and FOV constraints and realizing QPI with a high spatial bandwidth product (SBP). As a new-generation non-interferometric computational imaging technology, FPM has been widely used in the fields of biomedicine and digital pathology because of its ability to achieve superior performance with a simple system, some examples include white blood cell counting and analysis [30,31] and pathological tests such as circulating tumor cells [32,33].

FPM has received extensive attention from researchers since it was proposed by Zheng *et al.* [22] in 2013, and a number of improvements have been proposed [34–36]. However, conventional FPM requires sufficient data redundancy (the spectral overlap of neighboring subapertures should be greater than 60%) [37] to ensure that the iterative algorithm converges and achieves better recovery results. Typically, we need to acquire a large number of low-resolution (LR) images (tens to hundreds), which dramatically increases the front-end acquisition time as well as the computational complexity of the back-end reconstruction process, resulting in a low imaging efficiency of FPM with respect to the temporal-spatial bandwidth product (SBP-T). Furthermore, in many QPI studies, asymmetric illumination strategies are used to reconstruct the phase information of the sample [20,38]. These limitations have hindered the application of FPM in *in vitro*, label-free, and real-time QPI.

To improve imaging efficiency, previous studies have adopted two approaches. In the first approach, the number of LR images captured is reduced by optimizing the sampling strategy, in which sparse sampling [37,39] sufficiently reduces the data redundancy requirement of the FPM, and the adaptive illumination sampling strategy [40], which analyzes the spectral energy distributions of the samples in different orientations to adaptively select the images that need to be captured according to the magnitude of the energy. In the second approach, in which parallel acquisition is used to reduce the number of acquired LR images, the two most representative methods are multiplexed coding illumination [41] and source-coded imaging [42], both of which realize fast acquisition and spectrum filling; however, in this type of method, the more LEDs are turned on in parallel, the more difficult the subsequent complex decoherence process is

[43], and the quality of the imaging is difficult to guarantee. Both of these approaches reduce to some extent the amount of data acquired by the FPM; however, tens of LR images must still be acquired to complete the reconstruction. In addition, for the application scenario of phase imaging, the DPC imaging method proposed by Tian *et al.* [20] uses the phase contrast generated by asymmetric semicircular illumination used in the bright-field (BF) range to achieve low-frequency phase recovery. Subsequently, Sun *et al.* [38] proposed a method based on annular illumination FPM (AI-FPM), which analyzes the optical transfer function during the imaging process, and concluded that low-frequency phase information can be better reconstructed when $NA_{ill} = NA_{obj}$; based on this, AI-FPM achieved fast imaging of in vitro living cells with only 4–12 LR images. However, the imaging resolutions of the two aforementioned methods do not yet exceed the incoherent diffraction pole ($2NA_{obj}$). Deep-learning-based reliable phase imaging methods require many raw FPM datasets to establish a priori knowledge and have increased prediction errors for FOVs outside of the training set [44]. Recently, Fan *et al.* [45] proposed an efficient synthetic aperture FPM (ESA-FPM) method, which used seven LR images to achieve a resolution of $3NA_{obj}$; however, it was not possible to obtain the phase information of the sample because incoherent illumination does not have a phase definition [26]. Therefore, high-throughput quantitative phase reconstruction of samples using a small number of acquired images is urgently required.

In this paper, first, we theoretically analyze the effect of using a parallel acquisition strategy on phase recovery in the BF low-frequency information ($NA_{ill} \leq NA_{obj}$) and dark-field high-frequency information ($NA_{ill} > NA_{obj}$) regions in the frequency domain. Second, we propose a fast QPM based on Fourier ptychography (FQP-FPM). The proposed method first performed annular downsampling of the conventional FPM. In the BF acquisition, we retained the original sequential acquisition scheme based on asymmetric illumination at the matched annular illumination position ($NA_{ill} = NA_{obj}$), which ensures accurate recovery of low-frequency phase information. In the DF acquisition ($NA_{ill} > NA_{obj}$), we adopted a parallel acquisition strategy based on symmetric illumination to achieve fast reconstruction of high-frequency phase information. Simultaneously, we propose novel phase-recovery algorithms that can match the aforementioned acquisition schemes and are capable of achieving fast convergence with a small number of acquired raw images. We verified the feasibility of the proposed FQP-FPM method through simulation experiments, applied it to observe unstained cell samples in vitro and achieved satisfactory results.

2. Methods

2.1. FQP-FPM forward imaging model

In the conventional FPM system shown in Fig. 1(a), the conventional microscope illumination source is replaced by an LED array located a distance h below the sample plane, and the illumination of any LED unit can be realized by the control system [22]. Conventional FPM activates the LED units sequentially to produce different angles of tilted plane wave $(u_m, v_m) = \left(\frac{\sin\theta_x^{(m)}}{\lambda}, \frac{\sin\theta_y^{(m)}}{\lambda} \right)$ (m denotes the LED cell and its subaperture index, λ is the illumination wavelength, and $\theta^{(m)}$ is the illumination aperture angle of the m^{th} LED cell in the figure) to illuminate the sample. We define the 2D complex-amplitude transmittance function of the sample as $s(x, y) = a(x, y)e^{j\Phi(x, y)}$, panning the sample spectral information beyond the objective bandwidth to within the objective bandwidth and simultaneously acquiring the corresponding LR image at the camera port, which can be expressed as

$$I_m(x, y) = |F^{-1}\{S(u - u_m, v - v_m) \cdot P(u, v)\}|^2, \quad (1)$$

where (x, y) and (u, v) denote the 2D real space and frequency-domain coordinates, respectively; F^{-1} denotes the 2D Fourier inverse transform; and $P(u, v)$ denotes the optical pupil function of

the objective lens, which is regarded as the coherence transfer function in the FPM, which in turn can be considered as a low-pass filtering function in the circular domain with radius $\frac{NA_{obj}}{\lambda}$:

$$P(u, v) = \begin{cases} 1, & (u^2 + v^2) \leq \left(\frac{NA_{obj}}{\lambda}\right)^2 \\ 0, & \text{otherwise} \end{cases}. \quad (2)$$

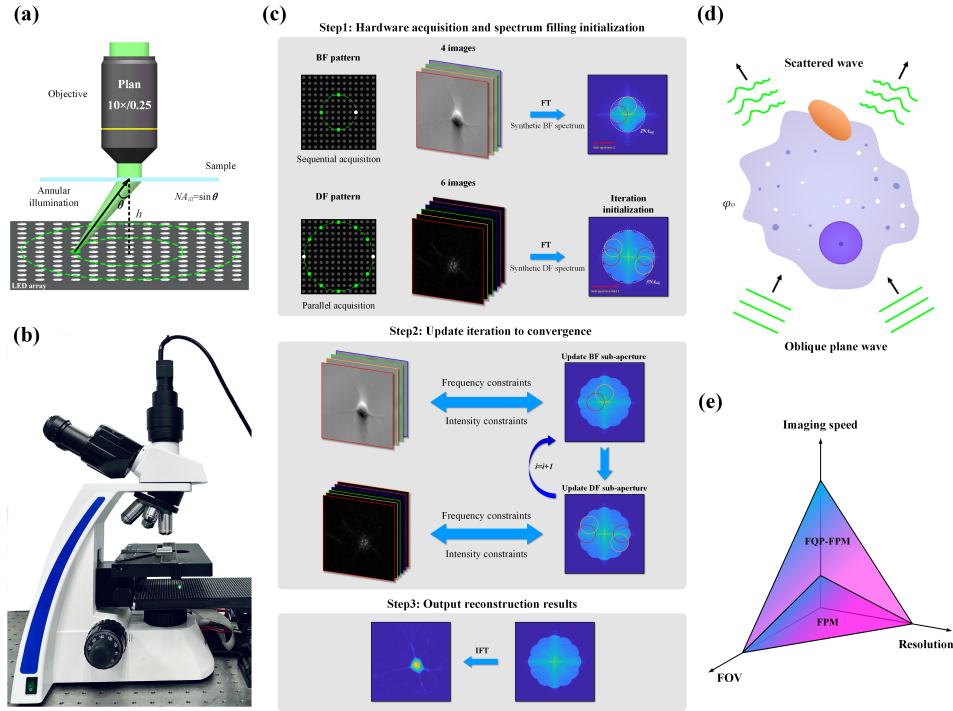


Fig. 1. FQP-FPM hardware implementation, working flow, phase delay, and SBP-T. (a) Setup of the FQP-FPM system based on a biomicroscope equipped with a programmable LED array source. (b) Image of the FQP-FPM experimental platform. (c) Flowchart of the data acquisition and reconstruction process in FQP-FPM of simulated cell phase samples. (d) Phase delay produced by an oblique coherent illumination plane wave through a sample. (e) Time-space bandwidth product of FPM and FQP-FPM.

Therefore, a series of LR images acquired at the camera port represent the subregion information of the sample in different frequency-domain spaces. The subspectra of the samples are spliced and expanded using an FP algorithm based on the framework of the alternating iteration algorithm [46] to achieve a larger synthetic aperture: $NA_{syn} = NA_{obj} + NA_{ill}$, where NA_{ill} is the maximum illumination aperture in the target direction and $NA_{ill} = \sin(\theta_{max})$. In addition, owing to the characteristics of coherent illumination, the phase information of the sample at different spatial locations is preserved [26]. Then, the FP algorithm alternates the projection in the spatial and Fourier domains to estimate the constraint, and the optimal solution is ultimately derived by iterating until convergence; the error can be expressed as follows:

$$E(k) = \sum_n \sum_{x,y} |I_m(x, y) - |F^{-1}\{S(u - u_m, v - v_m) \cdot P(u, v)\}|^2|^2. \quad (3)$$

As a result, FPM can theoretically achieve several times the resolution of the coherent diffraction limit as well as phase reconstruction. However, FPM relies on a large number of raw datasets

that are generated by a large number of illumination angle scans (hundreds of LR images may need to be acquired) [37], which severely reduces the SBP-T of FPM, as shown in Fig. 1(e).

Our experimental setup is based on a modification of the conventional FPM, as shown in Fig. 1(a) and (b). Step 1 in Fig. 1(c) demonstrates our hardware acquisition process, where we separately acquired LR images of BF and DF. The white LED unit represents the LED illumination mode in a one-shot exposure. In the BF, we set up four LED units in an annular configuration, sequentially illuminated the samples, and acquired four BF images. In the DF, we set up a symmetric illumination of the samples with 12 LED units and acquired six DF images. Finally, only ten LR images were collected as the pre-reconstruction dataset, which significantly reduced the amount of data compared to conventional FPM acquisition and improved the SBP-T of the FPM. The specific lighting strategy and the reconstruction process are described next.

2.2. Illumination and acquisition strategy of the FQP-FPM

Before discussing the illumination strategy of the FQP-FPM method, we first clarify the definitions of BF and DF illumination in the FPM system in the frequency domain, taking the spectrum of the object function of the sample, $S(u, v)$, as an example.

$$\begin{cases} \sqrt{(u)^2 + (v)^2} \leq \frac{NA_{obj}}{\lambda}, & \text{BF} \\ \sqrt{(u)^2 + (v)^2} > \frac{NA_{obj}}{\lambda}, & \text{DF} \end{cases} \quad (4)$$

When the wavelength λ of the illumination light is determined, the spectral ranges of BF and DF are determined only by NA_{obj} . Therefore, as shown in Fig. 2, we defined the BF spectral range as the light-blue circular area, which represents the spatial location distribution of the low-frequency information, and the DF spectral range as the white area outside the light-blue circular area, which represents the spatial location distribution of the high-frequency information. When we turn on the m^{th} LED unit illumination sample, the acquired LR image can be considered as the information of the sample intercepted at different frequency-domain locations using a subaperture with radius NA_{obj} (only NA is discussed when λ is determined). Therefore, we further determined whether a BF exists in the acquired images.

$$\begin{cases} \sqrt{(u_m)^2 + (v_m)^2} < \frac{2NA_{obj}}{\lambda}, & \text{Existing BF} \\ \sqrt{(u_m)^2 + (v_m)^2} \geq \frac{2NA_{obj}}{\lambda}, & \text{No BF} \end{cases} \quad (5)$$

(u_m, v_m) can also be considered as the location of the center of the circular subaperture diameter, as indicated by the orange and purple circles in Fig. 2. When the length of the subaperture center from the coordinate origin is less than $2NA_{obj}$, the low-frequency information within the BF range is captured, and vice versa, the high-frequency information is completely DF. In addition, the dashed circles with different radii of the coordinate axes represent the target NA_{syn} spectrum coverage centered on the origin.

Here, we first annular downsample the conventional FPM for phase recovery. In this step, we set up two annular bands in the frequency-domain space, as shown in the first two rows of Fig. 2. The first annular band is located at $NA_{ill} = NA_{obj}$, and considering Eq. (5), we observe that the subaperture centered at this position contains half of the BF low-frequency information, and the acquired image can ensure good recovery of the low-frequency phase information and satisfy the spectral filling in the range of $2NA_{obj}$ [38]. The second annular band is located at $NA_{ill} = 2NA_{obj}$, and the subaperture centered at this position collects the high-frequency information of the full DF and satisfies the spectrum filling in the range of the target $3NA_{obj}$.

In the two annular bands, we set up 4 and 12 LEDs, and the LEDs in each annular band are distributed in the form of equally divided rounded corners to ensure uniform overlapping; the

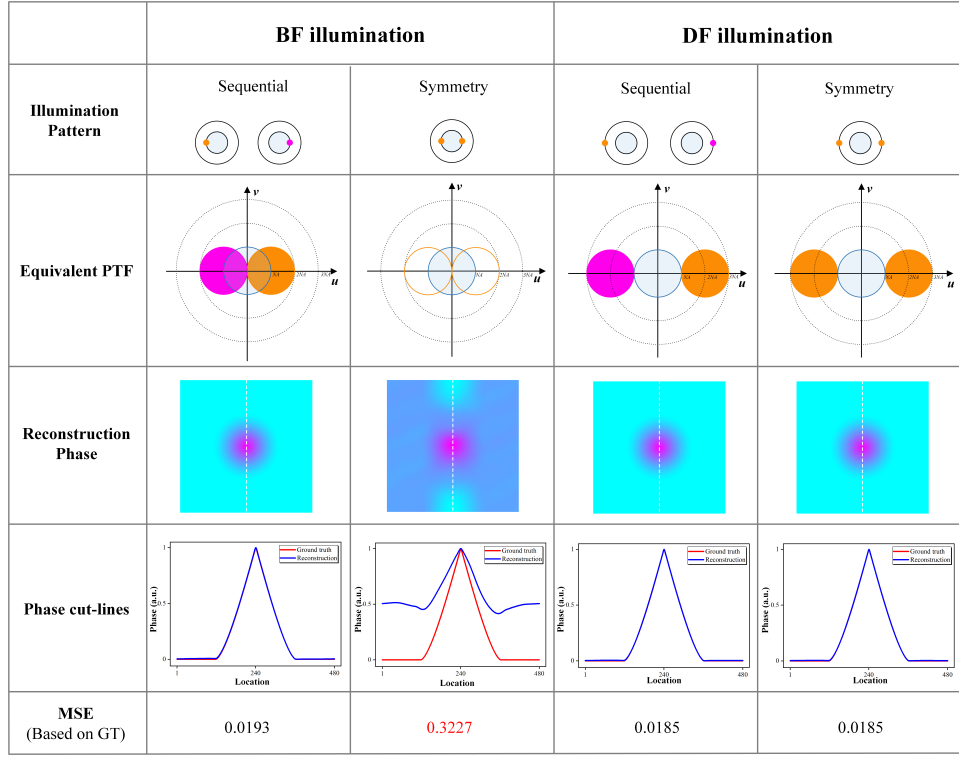


Fig. 2. Exploring the effect of using a symmetric-illumination-based parallel acquisition strategy on phase recovery at locations containing bright fields and completely dark fields.

hardware implementation of their corresponding spatial domains is shown in Step 1 of Fig. 1(c). At this point, we only need to acquire a total of 16 images (sequential acquisition) to realize the spectrum filling of the sample $3NA_{obj}$. Then, combined with the subsequent reconstruction algorithm to realize the phase reconstruction, this stage-by-stage scheme is used as the QP-FPM acquisition strategy.

To further minimize the acquired LR images, it may be necessary to consider the use of a parallel acquisition strategy, where the illumination is considered partially coherent when we turn on multiple LED units (assuming that there is no overlap in the Fourier domain) and the plane waves from the different LEDs are considered to be independent of each other. Therefore, the subimage captured via parallel acquisition can be considered as a superposition of the respective coherent states [41]:

$$I_{N,m}(x,y) = \sum_{n=1}^N |\mathcal{F}^{-1}\{S_n(u-u_m, v-v_m) \cdot P(u,v)\}|^2, \quad (6)$$

where $n = 1, 2, 3, \dots, N$ is the number of LEDs turned on in parallel and N is its upper limit. However, because the difference in illumination intensity between BF and DF can be hundreds of times, if a mix-and-match scheme of BF and DF illumination is used (which allows parallel illumination of more LEDs) [42], the weakly scattered light signals acquired in the DF will be overwhelmed by the noise in the BF, and excessive demixed coherent state multiplexing will be risky [43], which is not conducive to subsequent reconstruction recovery. Therefore, parallel acquisition based on symmetric illumination can be used in FPM as a strategy with a simpler demultiplexing process.

Previously, asymmetric sequential illumination strategies were commonly used to reconstruct the phase information of a sample [20,38]. However, we found that asymmetric sequential illumination is not the only solution for the reconstruction of high-frequency phase information of samples and that a parallel acquisition strategy based on symmetric illumination also achieves near-equivalent reconstruction results and can further reduce the number of acquired LR images. The prerequisite is that the corresponding acquired subaperture must not contain any BF low-frequency information, that is, a full DF image, as defined in Eq. (5).

Therefore, as shown in Fig. 2, we discuss the use of symmetric illumination for BF and DF in terms of FPM phase reconstruction, and we simulate ideal pure-phase microspheres to explore the phase-reconstruction effects of the two illumination strategies. In particular, note that based on the application scenario discussed in this study (label-free phase imaging of transparent samples), we define a pure-phase sample as: $s(x, y) = e^{j\Phi(x, y)}$. Here we use the mean-square-error (MSE) factor as an objective metric for evaluating reconstructed phase images. The LED illumination strategy is shown in the first row of Fig. 2. First, a simulation analysis is performed for the two illumination modes, including BF (for example, in this study, the center of the circle is located at $NA_{ill} = NA_{obj}$), and the results are shown in the third to fifth rows of Fig. 2. The reconstructed phases of the asymmetric sequential illumination strategy are close to the ideal phases (smaller MSE values), the reconstructed images of the symmetric illumination strategy show a large error (larger MSE), and it can be assumed that the phase information cannot be successfully reconstructed in the general case. We defined the equivalent phase transfer function (PTF) of the two illumination strategies based on the simulated phase-reconstruction results, as shown in the second row of Fig. 2, where a solid circle represents the use of this illumination strategy to obtain the subaperture information at that frequency-domain location as favorable for phase reconstruction; conversely, a hollow circle represents unfavorable phase reconstruction.

The use of images with BF symmetric illumination severely affects the reconstruction of low-frequency phase information. To avoid confusion, we adopt sequential illumination to ensure the successful recovery of low-frequency phase information before discussing the reconstruction of high-frequency phase information of DF (for example, the center of the circle is located at $NA_{ill} = 2NA_{obj}$). As shown in the third and fourth columns of Fig. 2, the reconstructed phases are close to the ground truth (GT) (All MSE values are small), regardless of whether sequential or symmetric illumination is used. The phases can be successfully reconstructed theoretically, and their equivalent PTFs are all represented as solids. This preliminarily demonstrates the feasibility of a parallel acquisition strategy based on symmetric illumination for DF high-frequency phase reconstruction.

In QPI, the acquired image needs to possess phase-contrast information (qualitative characterization of phase information) before it is possible to quantitatively reconstruct the phase information of the sample using a phase-recovery algorithm. In BF-based transmitted light-field imaging models, this requires asymmetric illumination to break the symmetry in order to produce a strong phase contrast for quantitative phase reconstruction, such as the FPM and DPC method. However, the DPC method cannot be generalized to DF due to the need for the presence of a strong reference wave in the bright field [20]. In contrast, in DF imaging, due to the limited angle of the transmitted light collected by the objective lens NA, the information brought by the large-angle tilted illumination of the DF mainly comes from Rayleigh or Mie scattering of light interacting with matter, as shown in Fig. 1(d). At this point, either with asymmetric or symmetric illumination, the scattered information captured by the dark field will carry the phase lining information of the sample, which is significantly different from the case of BF transmitted light imaging, as can be seen in classical dark-field microscopy with a circularly symmetric light source. Label-free dark-field microscopy based on phase contrast generation via scattered light has been widely used in the imaging of thin cell samples [47–49]. Therefore, all FPMs can theoretically perform quantitative phase reconstruction of the high-frequency phase-contrast

information carried by these DF image by means of a phase-recovery algorithm. This is further discussed in the [Supplement 1](#).

For the fast acquisition of high-frequency phase information and quantitative sample reconstruction, the results discussed in this section combined with Fig. 2 are sufficient to support the use of a symmetric-illumination-based parallel acquisition strategy in the second annular band (full DF position) on top of the QP-FPM acquisition strategy, which further halves the amount of data to be acquired by the DF acquisition; the final total number of LR images to be acquired is determined to be 10, which we refer to as the FQP-FPM acquisition strategy. The specific imaging effect comparison is discussed in detail in Section 3.

2.3. FQP-FPM reconstruction algorithm

After introducing the FQP-FPM illumination and acquisition strategy, we preliminarily explored a fast acquisition strategy that facilitates phase reconstruction. However, at the same time, we need an FP reconstruction algorithm that can meet the requirements. Conventional FP reconstruction algorithms based on alternating iterations may fail to converge with a low reconstruction quality in the case of a small number of acquisitions and low data redundancy. Therefore, we propose the FQP-FPM phase-recovery algorithm, which aims to achieve fast convergence and high-quality reconstruction with a small number of acquisitions, the reconstruction process is shown in Fig. 1(c).

Before performing iterative reconstruction, it is necessary to perform noise reduction on the acquired LR images to minimize the impact of noise on the reconstruction quality. Here, we determine the threshold value by calculating the arithmetic mean intensity difference between the target and actual acquired images [50]: $Threshold_m = \langle I_{N,m}(r) \rangle - \langle I_t(r) \rangle$, and we perform noise reduction as follows:

$$I_{N,m}^d(r) = I_{N,m}(r) - Threshold_m, \quad (7)$$

where $I_{N,m}^d(r)$ denotes the LR image after noise reduction; for convenience, we set $r = (x, y)$ as the spatial-domain coordinates and $k = (u, v)$ as the frequency-domain coordinates. Subsequently, the LR images obtained after noise reduction were used for spectrum filling and iterative initialization. The four acquired BF LR images were Fourier transformed to complete the spectrum filling of low-frequency information. Then, the six acquired DF LR images are Fourier transformed to complete the spectrum filling of the high-frequency information (one DF LR completes the filling of the two symmetric positions of the subaperture), and the filled spectrum and its solution phase will be used as the initialized HR spectrum and guess for the subsequent iterations, respectively, which labeled as $S^0(k)$, and $S^{(i)}(k)$ represents the sample HR spectrum of the i^{th} iteration. Subsequently, the iterative updating starts, which first requires frequency-domain constraints. A spectral shift is generated after the sample is illuminated by incident wave vectors with different angles, which can be expressed as an interception of the corresponding subspectral region using the optical pupil function $P(k)$:

$$\phi_{N,m}(k) = \sum_{n=1}^N S(k - k_m) \cdot P(k). \quad (8)$$

The DF image is constrained simultaneously using two symmetric subapertures and then Fourier inverted back to the spatial domain: $\psi_{N,m}(r) = |\mathcal{F}^{-1}\{\phi_{N,m}(k)\}|^2$, which is equivalent to inverting the LR image acquired at the camera port. The next step is to perform intensity constraints; the phase of the sample complex amplitude is preserved, and amplitude replacement is performed using the acquired LR image:

$$\varphi_{N,m}(r) = \sqrt{I_{N,m}^d(r)} \frac{\psi_{N,m}(r)}{|\psi_{N,m}(r)|}. \quad (9)$$

Subsequently, it is Fourier varied back to the frequency domain: $\phi'_{N,m}(k) = \mathcal{F}\{\varphi_{N,m}(r)\}$. The sample HR spectrum is then updated; to achieve fast convergence of the algorithm while obtaining a small number of LR images, we improve the iterative engine of ePIE [28,46] by introducing an adaptive modulation factor α to optimize the spectrum update strategy, as follows:

$$\alpha = 2(|P(k + k_m)|_{\max}) - \frac{\sum_{m=1}^M \text{Threshold}_m}{M}, \quad (10)$$

$$S_{m+1}(k) = S_m(k) + \left(\alpha - \frac{|P(k + k_m)|}{|P(k + k_m)|_{\max}} \right) \frac{P_m^*(k + k_m)}{|P_m(k + k_m)|^2 + \delta} [\phi'_{N,m}(k) - \phi_{N,m}(k)], \quad (11)$$

where δ is the regularization parameter, * represents the conjugate operation, and $\frac{\sum_{m=1}^M \text{Threshold}_m}{M}$ denotes the average arithmetic threshold of the LR image dataset. The algorithm must update all LR images to be considered as completing one iteration, iteratively converging to the optimal solution according to Eq. (3). Finally, the Fourier inverse transforms the HR spectra of the samples back into the spatial domain. This is summarized in Algorithm 1.

Algorithm 1. FQP-FPM reconstruction algorithm

Input: A set of LR images $I_{N,m}(r)$

Output: Recovered object complex distribution x

Pretreatment: Use Eq. (7) to obtain denoised LR images $I_{N,m}^d(r)$

Initialization: Spectrum filling using $I_{N,m}^d(r)$ and initialize $S^0(k)$

while not converged **do**

for $m = 1$ to M (different measurements)

 1) Frequency-domain constraints: Calculate $\phi_{N,m}(k)$ according to Eq. (8)

 2) Amplitude constraints: Calculate $\varphi_{N,m}(r)$ according to Eq. (9)

 3) Update the sample HR spectrum and calculate $S_{m+1}(k)$ using the improved spectrum update strategy according to Eq. (10) and Eq. (11)

End

$S^{(i)}(k) \leftarrow S^{(i+1)}(k)$

 Determine convergence according to Eq. (3)

end while

return $x = \mathcal{F}^{-1}\{S^{(i)}(k)\}$

3. Experiments and results

3.1. Validation of the FQP-FPM via simulation experiments

To verify the imaging effect of FQP-FPM, we simulated pure-phase samples (USAF) to accurately verify the feasibility of the proposed FQP-FPM method for fast quantitative phase reconstruction and compared it with the conventional FPM method, as shown in Fig. 3(a). All simulation experiments were performed on an experimental platform with a $4\times/0.1$ NA objective lens, camera with an image size of $2.4\ \mu\text{m}$, central illumination wavelength of 531 nm, and adjacent spacing of 2.5 mm for the LED array. The LED array, simulated by the conventional FPM method, was located at 86.5 mm below the sample, the spectral overlap rate was controlled at 83.28% to ensure the reconstruction quality, a central 15×15 LED unit was chosen to sequentially illuminate the sample, and 225 LR images were used to complete the $3NA_{obj}$ spectrum filling, as shown in Fig. 3(c1). The distance from the LED array to the sample simulated using the other methods was 49.5 mm, and the radii of the first and second annular rings were set to 5 and 10 mm, respectively. Figure 3(b) shows the reconstruction effect of the QP w/o DF method

(QP-FPM method without DF illumination), which uses four LR images (asymmetric sequential illumination) to realize the horizontal and vertical spectral filling of $2NA_{obj}$. The low-frequency phase information of the phase samples could be better reconstructed because the subaperture centers were matched with NA_{obj} , as shown in Fig. 3(b2)–(b3) [38]. Figure 3(b1) shows that the spectrum filling within $2NA_{obj}$ is partially missing, which may cause the method to be less dominant than other methods that implement $2NA_{obj}$. Figure 3(d1) shows the spectrum reconstructed using the QP-FPM method with 16 LR images.

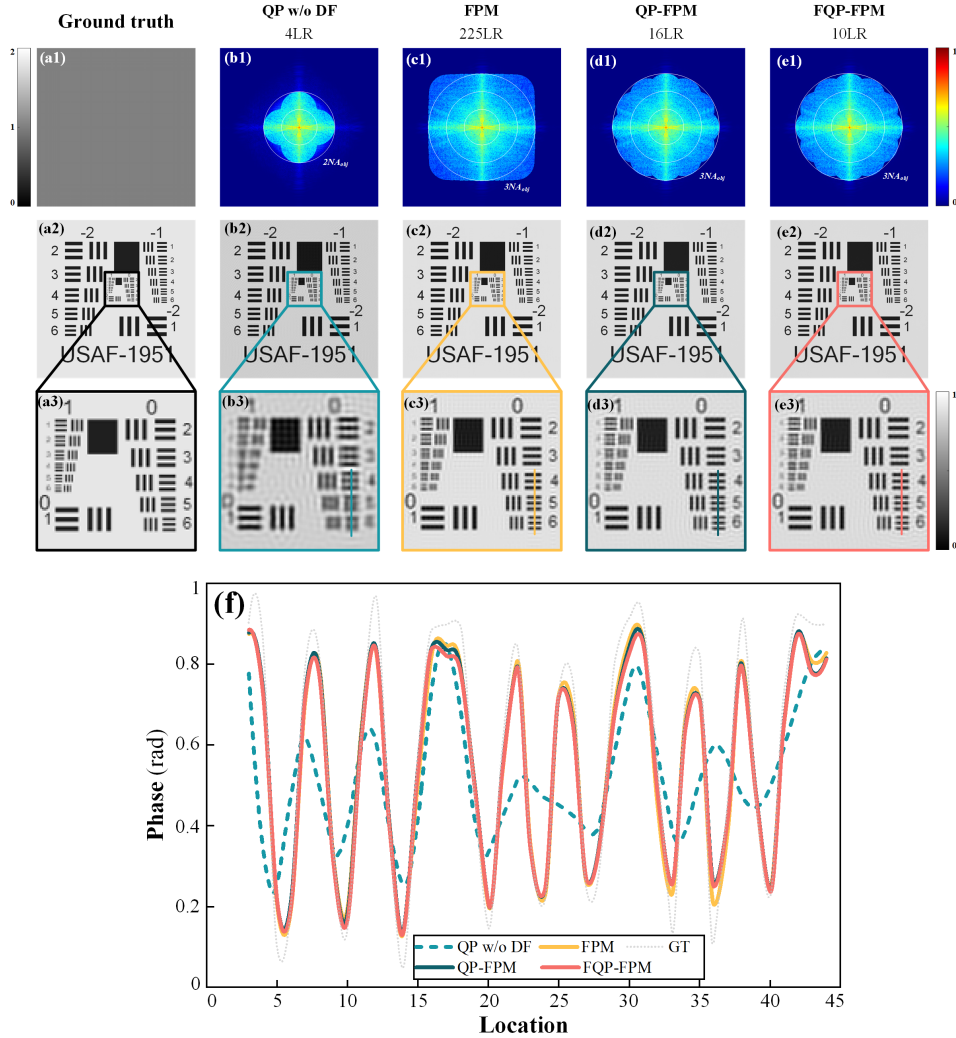


Fig. 3. FQP-FPM Validation via pure-phase sample (USAF) reconstruction in simulation experiments. (a) Ground-truth amplitude and phase images of the complex transmittance function used to simulate the sample. (b) Spectrum and phase reconstruction using QP-FPM without dark-field illumination (QP without DF). (c) Spectrum and phase of conventional FPM reconstruction. (d) Spectrum and phase of QP-FPM reconstruction. (e) Spectrum and phase of FQP-FPM reconstruction. (f) Comparison of normalized pixel value curves of labeled regions of interest for four reconstruction phase methods.

Because the illumination of the DF position is set to $NA_{ill} = 2NA_{obj}$, which does not have any low-frequency information of the BF, it can quickly realize spectral filling of $3NA_{obj}$ and simultaneously fill in the missing information in $2NA_{obj}$, and it can have a good coverage of the spectrum in all directions. The reconstruction effect of QP-FPM shown in Figs. 3(d2)–(d3) is close to that of the conventional FPM method. Figure 3(e1) shows the reconstruction results of FQP-FPM using a parallel acquisition scheme based on symmetric illumination at DF locations, which achieves spectrum filling more quickly at the DF locations. As shown in Figs. 3(e2)–(e3), the reconstruction effect is close to that of QP-FPM and conventional FPM; however, the proposed method only acquires ten LR images, which substantially improves the imaging efficiency of the FPM method. Figure 3(f) shows the normalized phase profile curves of the aforementioned four methods in the labeled out; evidently, the QP w/o DF method is significantly weaker than the other methods because of the spectral filling of the $2NA_{obj}$ alone. The resolution ability is obviously weaker than that of the other methods, and for the QP and FQP methods, the curves are closer than those of the conventional FPM methods in general and in detail. In addition, to further quantify the comparison between curves, we compared the curves in Fig. 3(f) with the reconstructed phase results, and the similarity values with GT are listed in Table 1; a higher curve similarity and SSIM index represent results closer to those of GT. Evidently, owing to the lack of a synthetic aperture, the QP w/o DF method resulted in the lowest curve similarity index and SSIM (68.65% and 0.8947, respectively), whereas the conventional FPM, QP-FPM, and FQP-FPM methods all realized the spectrum filling of $3NA_{obj}$, and their curve similarities (99.01%, 98.94%, and 98.91%, respectively) were closer to the SSIM index (0.9610, 0.9571, and 0.9567, respectively). This verifies the quality of the quantitative phase reconstruction of FQP-FPM with a small number of acquisitions. Please see the [Supplement 1](#) for details on the exploration of the data redundancy requirements of the FQP-FPM method and simulations in the presence of noise in the experiment. In addition, FQP-FPM not only achieves high-quality reconstruction of the phase for complex amplitude samples but also recovers of the intensity information of the samples, as also demonstrated in the experiments in [Supplement 1](#). All things considered; the proposed method is currently the most efficient phase imaging improvement for FPM in exceeding the incoherent diffraction limit.

Table 1. Spectral coverage, data requirements, and quantitative profile curve similarity and structural similarity of the reconstructed phases for four methods (based on GT)

	QP w/o DF	FPM	QP-FPM	FQP-FPM
Spectrum coverage	$2NA_{obj}$	$3NA_{obj}$	$3NA_{obj}$	$3NA_{obj}$
Data requirements (Number of LR)	4	225	16	10
Curve similarity (Based on GT)	68.65%	99.01%	98.94%	98.91%
SSIM (Based on GT)	0.8947	0.9610	0.9571	0.9567

3.2. Resolution benchmarking of the FQP-FPM with USAF-1951 targets

To experimentally demonstrate the resolution performance of the FQP-FPM method, we used the resolution target of the United States Air Force (USAF-1951) as a sample to quantitatively characterize the imaging resolution. The parameters of this experiment were consistent with those in the simulation, and the experimental platform was built using a common research-grade biomicroscope system, as shown in Fig. 1(b). Figure 4(a) shows the 2.27-mm² large-FOV imaging of the USAF-1951 target captured under central coherent illumination with a 4×/0.1 objective. Figure 4(a1) shows a zoomed-in ROI for elements of Groups 6 and 7, where we canmore easily find the line pairs (Group 7-4) corresponding to the coherent diffraction limit (NA_{obj}) of the system, which corresponds to a resolution of 2.76 μm (blue squares and text

were used for labeling). The yellow boxes represent the elements of Groups 8 and 9, which have a much higher resolution and we zoomed in on, as shown in Fig. (a2). Figures 4(b)–(e) show the phase-reconstruction results of the QP w/o DF, conventional FPM, QP-FPM, and FQP-FPM methods, respectively (all of which are consistent with the parameters described in the simulation experiments in Section 3.1). We uniformly drew quantitative phase curves for Groups 8–2–8–6 on the right side, showing line pairs corresponding to the imaging resolution limits of the various methods, and drew the corresponding quantitative curves in the gray bottom portion for easy comparison. In addition, we show the line pairs corresponding to the imaging resolution limits of each method in the bottom part, drew the corresponding quantitative curves, and normalized all results to facilitate the comparison. As shown in Fig. 4(b), the limiting imaging line pairs for the QP w/o DF method is Group 8–4 ($1.38\ \mu\text{m}$), with double the resolution of the systematic coherent diffraction limit achieved under matched illumination conditions, i.e., $NA_{\text{syn}} = 0.2$. Figure 4(c) shows the phase-reconstruction results of the FPM method for conventional matrix illumination, where $NA_{\text{syn}} = 0.3$, achieving a resolution in the triple coherent diffraction limit (Group 9–1, $0.92\ \mu\text{m}$). Figure 4(d) shows the QP-FPM reconstructed phase results after using annular downsampling with the same limiting resolution as in the conventional FPM method. The reconstruction result of FQP-FPM is shown in Fig. 4(e), which uses the parallel acquisition strategy based on annular downsampling; its resolution effect is comparable to that of the conventional FPM and QP-FPM methods; however, FQP-FPM realizes the resolution of $3NA_{\text{obj}}$ more quickly.

In addition, we compared the amount of data required to be acquired at the front end (orange) with the reconstruction time at the back end (green) for the conventional FPM, QP-FPM, and FQP-FPM methods. As shown in Fig. 4(f), the front end of the conventional FPM method requires the highest amount of data acquisition (225 LR images), which leads to a larger computational complexity of the back-end reconstruction and a reconstruction time of 91.22 s. The QP-FPM after annular downsampling requires only 16 LR images, and its back-end reconstruction time is only 3.85 s, whereas the FQP-FPM requires only ten LR images and a reconstruction time of only 3.15 s (4.4% and 3.3% of those of the conventional FPM, respectively), which are the lowest values among the three methods. This experiment demonstrates the great potential of FQP-FPM in terms of imaging speed while achieving the theoretical resolution.

3.3. Imaging of unstained 293 T cells by the FQP-FPM method

After validating the imaging resolution of the FQP-FPM method, we further demonstrate its potential for application in the life sciences. In this experiment, unstained 293 T (human kidney epithelial) cells (pure-phase samples) were imaged to validate the feasibility of label-free QPI. We removed the normal surviving 293 T cells from the incubator and placed them in a liquid medium to allow them to grow slowly on the subappressed wall. To better observe the subcellular structure, this experiment used a $10\times/0.25\ \text{NA}$ objective lens, a camera with an image element size of $3.1\ \mu\text{m}$, and an LED array located at 44.00 mm directly below the sample, with a spacing of 4 mm between neighboring LED units. The radii of illumination of the first and second rings of the annulus were set to 12 and 24 mm, respectively, the illumination wavelength was kept constant, and the maximum achievable synthetic aperture was 0.75 NA. Figure 5(a) shows a $1.21\ \text{mm}^2$ large-FOV image captured under coherent point source illumination. Typically, owing to the uneven thickness and refractive index of the living cells, their main information is embedded in the phase, and the FPM method with high-throughput phase imaging capability requires a long time to complete the acquisition process because of the large amount of data collected at the front end, which is not conducive to the rapid phase imaging of living cells (both cells and medium are in microdynamics) and is prone to motion blurring [51].

Figures 5(b)–(e) show the phase imaging effects of the four ROIs shown in Fig. 5(a). Figures 5(b1) and 5(c1) show magnified views of ROIs 1 and 2. Owing to the advantages of LED

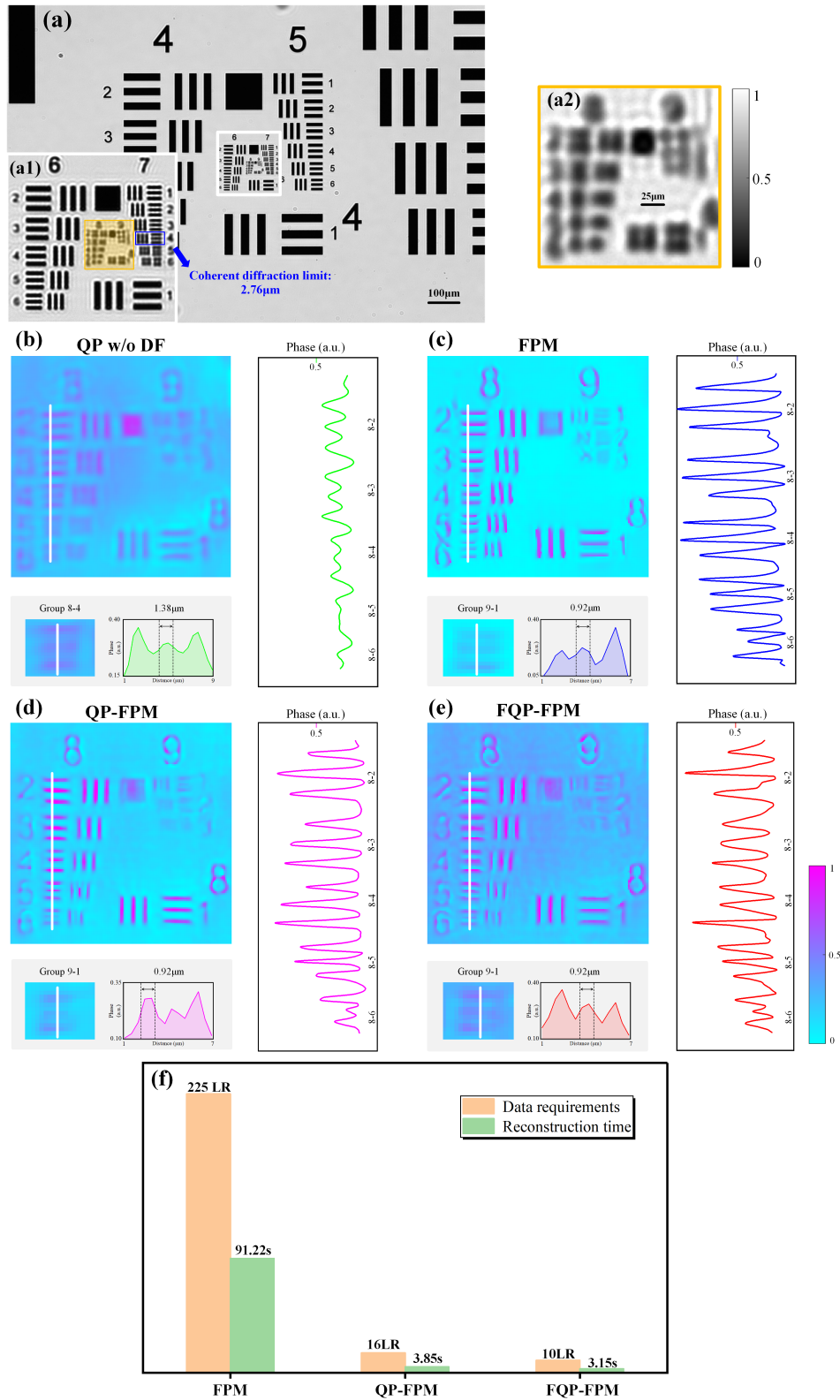


Fig. 4. High-throughput phase imaging results of the USAF-1951 resolution target. (a) Low-resolution (LR) bright field (BF) in-focus intensity image of USAF captured under a large FOV of $\sim 2.27 \text{ mm}^2$. (a1) Zoomed-in ROIs for the line pairs of Groups 6 and 7. (a2) Zoomed-in ROIs for the line pairs of Groups 8 and 9. (b)–(e) Phase-reconstruction results using the QP w/o DF, FPM, QP-FPM, and FQP-FPM methods, respectively, for Groups 8-2–8-6 and normalized quantitative phase curves for limit-resolution line pairs. (f) Front-end data volume versus back-end algorithmic reconstruction time for three methods (FPM, QP-FPM, and FQP-FPM) for reaching the triple coherent diffraction limit resolution of the system.

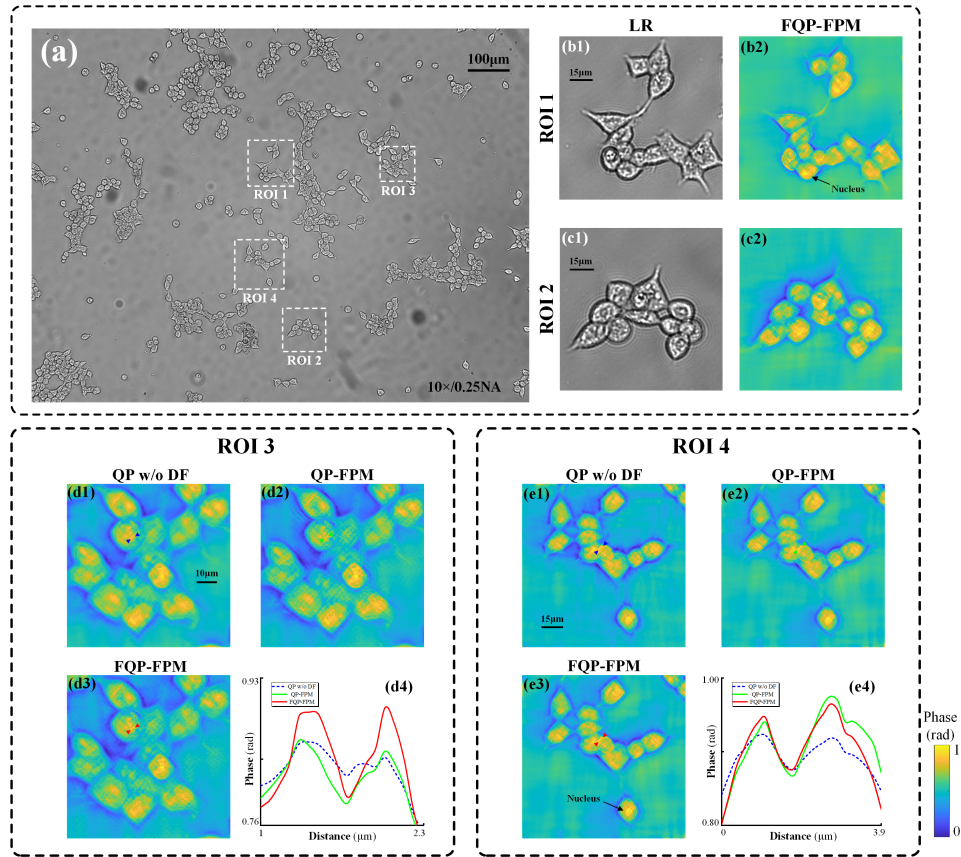


Fig. 5. QPI results for unlabeled 293 T cells. (a) Full FOV intensity image of 293 T cells collected under vertical illumination. (b) and (c) Amplification of ROIs 1 and 2 and their phase reconstruction results using the FQP-FPM approach. (d) and (e) Reconstruction of ROIs 3 and 4 using the QP w/o DF, QP-FPM, and FQP-FPM methods, respectively, and comparison of the quantitative phase profile curves at the resultant labels reconstructed using the three methods.

point source illumination, coherent illumination has better contrast and can initially transmit a stable bit phase difference [26]; however, owing to the diffraction limitation as well as the need for further synthesized aperture and phase reconstruction, the internal structure of the cell as well as detailed information cannot be observed. Figures 5(b2) and 5(c2) show the phase images of ROIs 1 and 2 reconstructed using the FQP-FPM method. Because of the realization of phase reconstruction at the $3\times$ coherent diffraction limit, the internal structure and information of the cell can be clearly presented. For example, in ROI 1, we can identify the nucleus, which is presented as a brighter cluster (with higher light transmittance) in the phase imaging, and endoplasmic reticulum on the outer surface, whereas the traditional method requires staining or fluorescent labeling according to the specific organelle to be observed normally. Figures 5(d)–(e) show the phase-reconstruction results of the QP w/o DF, QP-FPM, and FQP-FPM methods for ROIs 3 and 4. For the QP w/o DF method, as only four LR images were used to reconstruct the low-frequency phase information, the subcellular internal structure has to be further distinguished. In contrast, the QP-FPM method, which realizes $3NA_{obj}$ spectral coverage, accomplishes phase reconstruction of high-frequency information, and the inner cellular minutiae (labeled in the figure) can be better distinguished. Finally, the FQP-FPM method with a DF parallel acquisition

strategy achieves almost equivalent results to QP-FPM (both of their equivalent NAs are 0.75), which is consistent with the performance of the quantitative phase curves. It is worth noting that all reconstructions were normalized for comparison. In some cases, the FQP-FPM with a DF parallel acquisition strategy has better high-frequency details in the phase contrast, as shown in Fig. 5(d4) and (e4), while it only requires acquiring a minimum of ten LR images. These experimental results preliminarily verified that the FQP-FPM method can achieve in vitro imaging of living cells in a non-invasive manner.

3.4. *Imaging of unstained MARC-145 cells by the FQP-FPM method*

To further validate the capability of the FQP-FPM method for in vitro live-cell imaging, we performed non-invasive quantitative phase observations of MARC-145 cells (African green monkey embryonic kidney cells), which were also used as pure-phase samples. The parameters of this experiment as well as the basic operation remained unchanged from those presented in Section 3.3. As in the previous experiment, Fig. 6(a) shows a large-FOV image captured under coherent light source illumination and labeled with the four ROIs, and our reconstruction is shown in Figs. 6(b)–(e). While it is almost impossible to obtain effective information in conventional BF microscopy observation of clear cell samples, this issue is particularly prominent in Figs. 6(b2), 6(c2), 6(d1) and 6(e1). The FQP-FPM method can quantitatively reconstruct the phase of cells in a non-invasive manner, as shown in Figs. 6(b3) and 6(c3) corresponding to the reconstruction of ROIs 1 and 2, respectively, which both achieve 0.75 NA equivalent synthetic aperture. We can observe the cells in the normal growth state as well as the apoptotic cells (dashed circles), which are very strong owing to the increase in the permeability of the cell membrane. The apoptotic cells exhibit a very strong light transmission owing to the increased permeability of the cell membrane, and their corresponding light-range difference is in strong contrast to the other positions (reflected as “bright white”), based on which we observed the cell morphology of MARC-145 cells at different times. In addition, the “filamentous bands” connecting the cells can be easily identified as extracellular matrix proteins that mediate nutrient transport between cells [52]. Figures 6(d2) and 6(d3) show the phase and intensity images of ROI 3 reconstructed using the FQP-FPM method, which has the advantage of not only fast phase reconstruction owing to the illumination strategy but also intensity reconstruction. Figures 6(e2) and 6(e3) show the phase-reconstruction results of the QP w/o DF and FQP-FPM methods, respectively. As the phase reconstruction of the proposed FQP-FPM method breaks through the incoherent diffraction limit (three times the coherent diffraction limit), the high-frequency information is better resolved, as shown by the labeling of the reconstruction results and its phase normalization curve. In addition, we can observe the vacuolization of MARC-145 cells after a period of time out of the culture medium [53]. Finally, we visualized the 3D quantitative phase profiles of the reconstruction results presented in Fig. 6(b3), as shown in Fig. 6(f), which can further quantify the refractive index and thickness information of the cells. The aforementioned experimental results for biological samples demonstrate the performance and application potential of the proposed FQP-FPM method for high-throughput QPI, which is a powerful tool for future applications such as biological cell analysis and detection.

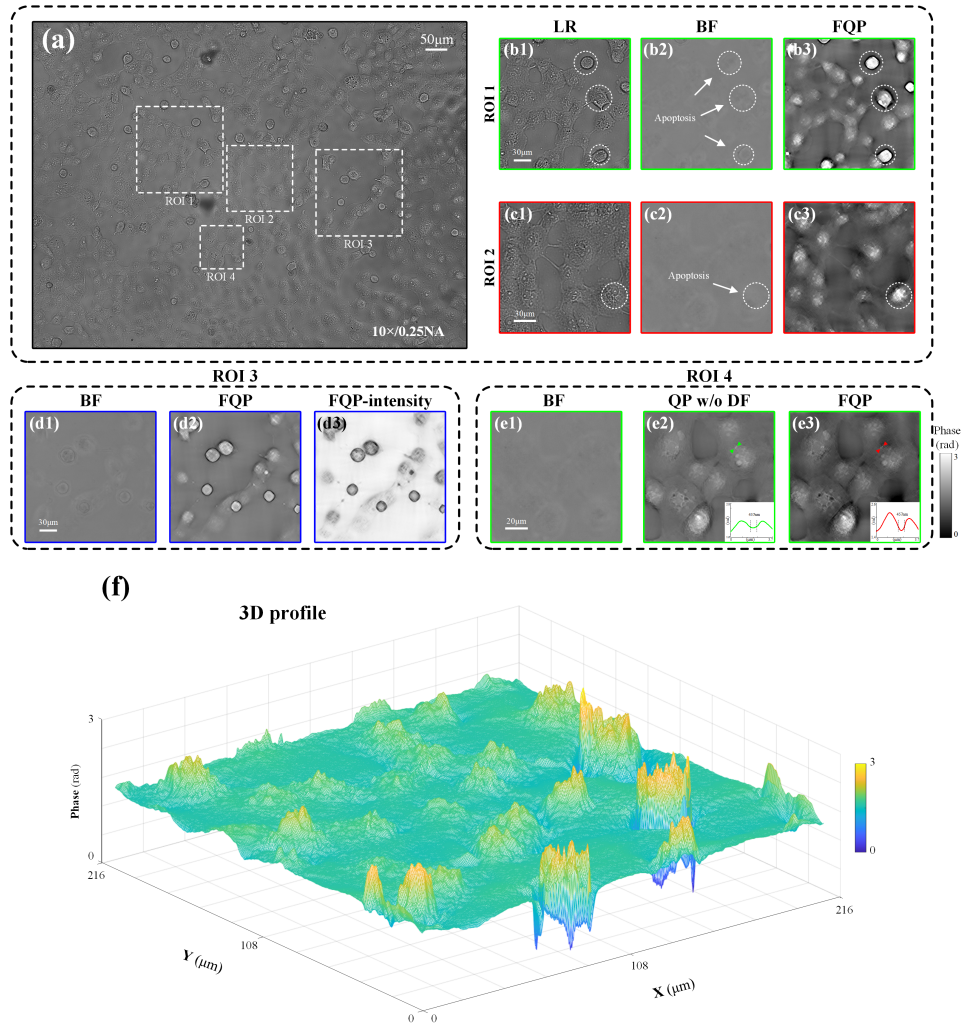


Fig. 6. QPI results of unlabeled MARC-145 cells. (a) Full FOV intensity image of MARC-145 cells collected under vertical illumination. (b), (c) Amplification of ROIs 1 and 2, BF illumination, and its phase-reconstruction results from the FQP-FPM approach. (d) ROI 3 image with BF illumination and phase and intensity reconstruction results for this location using the FQP-FPM method. (e) ROI 4 image under BF illumination and phase-reconstruction results for QP w/o DF with FQP. (f) 3D quantitative phase profile of the reconstruction results in (b3).

4. Discussion and conclusion

In this study, we proposed the FQP-FPM method, which is a fast, label-free, high-throughput, non-interferometric QPM imaging method. Our proposed method is based on annular downsampling of conventional FPM, and the acquisition strategies at BF and DF positions are discussed separately and analyzed theoretically and experimentally. We determined that an asymmetric sequential illumination strategy must be used as long as low-frequency BF information is involved [20,36], whereas a parallel acquisition strategy based on symmetric illumination can be used for complete DF positions to ensure high-frequency phase information recovery while realizing

fast acquisition. The results show that to achieve the same synthetic aperture as that achieved by conventional FPM, the proposed FQP-FPM method significantly reduces the data requirements for front-end acquisition and the computational reconstruction time for the back-end (4.4% and 3.3% of that of the conventional FPM, respectively), and no prior knowledge is required to be learned. In fact, the ideas of this study on acquisition strategies enable the proposed FQP-FPM to continue exploring the minimum data requirements for phase reconstruction at higher NA_{syn} values for biomedical applications with a higher imaging resolution and SBP-T. If the data requirements are to be further reduced (including avoiding the case of a quadratic increase in the amount of data), it may be necessary to combine the proposed method with improved demultiplexing algorithms [43,44], K-K relations [54], deep learning methods, and other computational imaging ideas (e.g., TIE and coded illumination) [18,42]. It is worth noting that the proposed FQP-FPM method also reconstructed the intensity information of the samples. However, compared with the intensity reconstruction of FPM, its quantitative phase reconstruction with improved performance is more valuable and promising for certain applications, particularly imaging applications such as in vitro unlabeled live biotransparent samples [33]. The front-end acquisition of conventional FPM is time-consuming, and it is difficult to realize real-time phase imaging; thus, reducing the data requirements of FPM is the most important indicator for real-time applications [23,24]. Therefore, the proposed FQP-FPM method dramatically improves the imaging efficiency of FPM in terms of phase, and its theory and method have landmark significance and value in advancing phase imaging research, which is expected to move towards clinical applications such as in the fields of bioimaging and life science detection. We will explore these research directions in future work.

Funding. Guangdong Provincial Key Field R&D Plan Project (2020B1111120004); Natural Science Foundation of Hubei Province (2022CFB099); Foshan University (2023 Annual Student Academic Fund, xsjj202305kja03).

Acknowledgment. We thank Dr. Pei for providing the live-cell samples in our experiments. We thank Prof. G. Zheng and other reviewers for their thoughtful suggestions and insights.

Disclosures. The authors declare no conflicts of interest.

Data availability. Data and code underlying the results presented in this paper are available from the corresponding author upon reasonable request.

Supplemental document. See [Supplement 1](#) for supporting content.

References

1. M. R. Costa, F. Ortega, M. S. Brill, *et al.*, "Continuous live imaging of adult neural stem cell division and lineage progression in vitro," *Development* **138**(6), 1057–1068 (2011).
2. K. Thorn, "A quick guide to light microscopy in cell biology," *Mol. Biol. Cell* **27**(2), 219–222 (2016).
3. M. Born, E. Wolf, A. B. Bhatia, *et al.*, "Electromagnetic Theory of Propagation, Interference and Diffraction of Light," in *Principles of Optics*, 7th ed. (Cambridge University Press, 1999).
4. S. W. Hell and J. Wichmann, "Breaking the diffraction resolution limit by stimulated emission: stimulated-emission-depletion fluorescence microscopy," *Opt. Lett.* **19**(11), 780–782 (1994).
5. K. Willig, S. Rizzoli, V. Westphal, *et al.*, "STED microscopy reveals that synaptotagmin remains clustered after synaptic vesicle exocytosis," *Nature* **440**(7086), 935–939 (2006).
6. E. Betzig, G. H. Patterson, R. Sougrat, *et al.*, "Imaging Intracellular Fluorescent Proteins at Nanometer Resolution," *Science* **313**(5793), 1642–1645 (2006).
7. S. T. Hess, T. P. K. Girirajan, and M. D. Mason, "Ultra-high resolution imaging by fluorescence photoactivation localization microscopy," *Biophys. J.* **91**(11), 4258–4272 (2006).
8. M. J. Rust, M. Bates, and X. W. Zhuang, "Sub-diffraction-limit imaging by stochastic optical reconstruction microscopy (STORM)," *Nat. Methods* **3**(10), 793–796 (2006).
9. B. Huang, W. Wang, M. Bates, *et al.*, "Three-dimensional super-resolution imaging by stochastic optical reconstruction microscopy," *Science* **319**(5864), 810–813 (2008).
10. Y. Park, C. Depeursinge, and G. Popescu, "Quantitative phase imaging in biomedicine," *Nat. Photonics* **12**(10), 578–589 (2018).
11. Y. Li, J. Di, K. Wang, *et al.*, "Classification of cell morphology with quantitative phase microscopy and machine learning," *Opt. Express* **28**(16), 23916–23927 (2020).

12. P. Marquet, B. Rappaz, P. J. Magistretti, *et al.*, "Digital holographic microscopy: a noninvasive contrast imaging technique allowing quantitative visualization of living cells with subwavelength axial accuracy," *Opt. Lett.* **30**(5), 468–470 (2005).
13. Z. Huang and L. Cao, "High Bandwidth-Utilization Digital Holographic Multiplexing: An Approach Using Kramers–Kronig Relations," *Adv. Photonics Res.* **3**(2), 2100273 (2022).
14. J. Liao, C. Zhang, X. Xu, *et al.*, "Deep-MSIM: Fast Image Reconstruction with Deep Learning in Multifocal Structured Illumination Microscopy," *Adv. Sci.* **10**(27), 2300947 (2023).
15. D. Li, L. Shao, B. C. Chen, *et al.*, "Extended-resolution structured illumination imaging of endocytic and cytoskeletal dynamics," *Science* **349**(6251), 447 (2015).
16. Z. Wang, L. Millet, M. Mir, *et al.*, "Spatial light interference microscopy (SLIM)," *Opt. Express* **19**(2), 1016–1026 (2011).
17. M. E. Kandel, C. Hu, G. N. Kouzehgarani, *et al.*, "Epi-illumination gradient light interference microscopy for imaging opaque structures," *Nat. Commun.* **10**(1), 4691 (2019).
18. C. Zuo, Q. Chen, W. Qu, *et al.*, "High-speed transport-of-intensity phase microscopy with an electrically tunable lens," *Opt. Express* **21**(20), 24060–24075 (2013).
19. J. Li, Q. Chen, J. Sun, *et al.*, "Optimal illumination pattern for transport-of-intensity quantitative phase microscopy," *Opt. Express* **26**(21), 27599–27614 (2018).
20. L. Tian and L. Waller, "Quantitative differential phase contrast imaging in an LED array microscope," *Opt. Express* **23**(9), 11394–11403 (2015).
21. J. Jiang, F. Li, F. Yang, *et al.*, "Single-shot color-coded LED microscopy for quantitative differential phase contrast imaging," *Opt. Laser Technol.* **161**, 109192 (2023).
22. G. Zheng, R. Horstmeyer, and C. Yang, "Wide-field, high-resolution Fourier ptychographic microscopy," *Nat. Photonics* **7**(9), 739–745 (2013).
23. G. Zheng, C. Shen, S. Jiang, *et al.*, "Concept, implementations and applications of Fourier ptychography," *Nat. Rev. Phys.* **3**(3), 207–223 (2021).
24. S. Jiang, P. Song, T. Wang, *et al.*, "Spatial-and Fourier-domain ptychography for high-throughput bio-imaging," *Nat. Protoc.* **18**, 2051–2083 (2023).
25. J. Kim, B. Henley, C. Kim, *et al.*, "Incubator embedded cell culture imaging system (EmSight) based on Fourier ptychographic microscopy," *Biomed. Opt. Express* **7**(8), 3097–3110 (2016).
26. J. W. Goodman and P. Sutton, "Introduction to Fourier optics," *Quantum and Semiclassical Optics-Journal of the European Optical Society Part B* **8**(5), 1095 (1996).
27. D. J. Lee and A. M. Weiner, "Optical phase imaging using a synthetic aperture phase retrieval technique," *Opt. Express* **22**(8), 9380–9394 (2014).
28. J. Luo, H. Tan, H. Chen, *et al.*, "Fast and stable Fourier ptychographic microscopy based on improved phase recovery strategy," *Opt. Express* **30**(11), 18505–18517 (2022).
29. M. Zhang, L. Zhang, D. Yang, *et al.*, "Symmetrical illumination based extending depth of field in Fourier ptychographic microscopy," *Opt. Express* **27**(3), 3583–3597 (2019).
30. A. Williams, J. Chung, X. Ou, *et al.*, "Fourier ptychographic microscopy for filtration-based circulating tumor cell enumeration and analysis," *J. Biomed. Opt.* **19**(6), 066007 (2014).
31. D. Wakefield, R. Graham, K. Wong, *et al.*, "Cellular analysis using label-free parallel array microscopy with Fourier ptychography," *Biomed. Opt. Express* **13**(3), 1312–1327 (2022).
32. A. Williams, J. Chung, C. Yang, *et al.*, "Fourier Ptychographic Microscopy for Rapid, High-Resolution Imaging of Circulating Tumor Cells Enriched by Microfiltration," in *Circulating Tumor Cells: Methods and Protocols in Molecular Biology*, vol 1634, (Humana Press, 2017).
33. A. Pan, C. Zuo, and B. Yao, "High-resolution and large field-of-view Fourier ptychographic microscopy and its applications in biomedicine," *Rep. Prog. Phys.* **83**(9), 096101 (2020).
34. R. Wu, J. Luo, J. Li, *et al.*, "Adaptive correction method of hybrid aberrations in Fourier ptychographic microscopy," *J. Biomed. Opt.* **28**(3), 036006 (2023).
35. C. Zheng, S. Zhang, D. Yang, *et al.*, "Robust full-pose-parameter estimation for the LED array in Fourier ptychographic microscopy," *Biomed. Opt. Express* **13**(8), 4468–4482 (2022).
36. Y. Shu, J. Sun, J. Lyu, *et al.*, "Adaptive optical quantitative phase imaging based on annular illumination Fourier ptychographic microscopy," *PhotonIX* **3**(1), 24 (2022).
37. J. Sun, Q. Chen, Y. Zhang, *et al.*, "Sampling criteria for Fourier ptychographic microscopy in object space and frequency space," *Opt. Express* **24**(14), 15765–15781 (2016).
38. J. Sun, C. Zuo, J. Zhang, *et al.*, "High-speed Fourier ptychographic microscopy based on programmable annular illuminations," *Sci. Rep.* **8**(1), 7669 (2018).
39. S. Dong, Z. Bian, R. Shiradkar, *et al.*, "Sparsely sampled Fourier ptychography," *Opt. Express* **22**(5), 5455–5464 (2014).
40. J. Luo, H. Tan, R. Wu, *et al.*, "Reduction in required volume of imaging data and image reconstruction time for adaptive-illumination Fourier ptychographic microscopy," *J. Biophotonics* **16**(3), e202200240 (2023).
41. L. Tian, X. Li, K. Ramchandran, *et al.*, "Multiplexed coded illumination for Fourier Ptychography with an LED array microscope," *Biomed. Opt. Express* **5**(7), 2376–2389 (2014).

42. L. Tian, Z. Liu, L. -H. Yeh, *et al.*, "Computational illumination for high-speed in vitro Fourier ptychographic microscopy," *Optica* **2**(10), 904–911 (2015).
43. S. Dong, R. Shiradkar, P. Nanda, *et al.*, "Spectral multiplexing and coherent-state decomposition in Fourier ptychographic imaging," *Biomed. Opt. Express* **5**(6), 1757–1767 (2014).
44. Y. Xue, S. Cheng, Y. Li, *et al.*, "Reliable deep-learning-based phase imaging with uncertainty quantification," *Optica* **6**(5), 618–629 (2019).
45. Y. Fan, J. Sun, Y. Shu, *et al.*, "Efficient synthetic aperture for phaseless Fourier ptychographic microscopy with hybrid coherent and incoherent illumination," *Laser Photonics Rev.* **17**(3), 2200201 (2023).
46. A. Maiden, D. Johnson, and P. Li, "Further improvements to the ptychographical iterative engine," *Optica* **4**(7), 736–745 (2017).
47. G. Zheng, C. Kolner, and C. Yang, "Microscopy refocusing and dark-field imaging by using a simple LED array," *Opt. Lett.* **36**(20), 3987–3989 (2011).
48. P. F. Gao, G. Lei, and C. Z. Huang, "Dark-field microscopy: recent advances in accurate analysis and emerging applications," *Anal. Chem.* **93**(11), 4707–4726 (2021).
49. R. Shi, X. Chen, J. Huo, *et al.*, "Epi-illumination dark-field microscopy enables direct visualization of unlabeled small organisms with high spatial and temporal resolution," *J. Biophotonics* **15**(1), e202100185 (2022).
50. L. Hou, H. Wang, J. Wang, *et al.*, "Background-noise reduction for Fourier ptychographic microscopy based on an improved thresholding method," *Curr. Opt. Photonics* **2**(2), 165–171 (2018).
51. L. Bian, G. Zheng, K. Guo, *et al.*, "Motion-corrected Fourier ptychography," *Biomed. Opt. Express* **7**(11), 4543–4553 (2016).
52. R. P. Mecham, "Overview of extracellular matrix," *Curr. Protoc. Cell Biol.* **57**, (2012).
53. A. V. Shubin, I. V. Demidyuk, A. A. Komissarov, *et al.*, "Cytoplasmic vacuolization in cell death and survival," *Oncotarget* **7**(34), 55863–55889 (2016).
54. Y. Baek, K. Lee, S. Shin, *et al.*, "Kramers–Kronig holographic imaging for high-space-bandwidth product," *Optica* **6**(1), 45–51 (2019).